

temperature. The biaxiality order parameter of the BC molecules can then be written as

$$\eta = \langle \cos 2\phi \rangle \quad (1)$$

where  $\phi$  is the azimuthal angle made by the long axis of the BC molecule with the  $\hat{b}$  director.

For the alignment of the BC molecules as shown in Fig. 4B, we can estimate the expected values of  $\mu_b - \mu_c$  using the polarizabilities of the two arms of the BC molecules and those of the background rod-like molecules, and the composition of the mixture. Assuming  $\eta$  to be  $\sim 0.3$ , we get  $\mu_b - \mu_c \approx 0.007$  for a concentration of 4.5% of the BC molecules, a value close to that measured at  $T_{ub} - T \approx 10^\circ\text{C}$ . However, if the BC molecules are vertically aligned, as in Fig. 4A, the value of  $\mu_a - \mu_c$  would be about one-third as great. The birefringence data in the temperature range of  $T_{ub}$  to  $T_{ub} - 0.15^\circ$  were fitted to the expression

$$\mu_b - \mu_c = C(T_{ub} - T)^\beta \quad (2)$$

using a nonlinear least squares fitting procedure (where  $C$  is a proportionality constant and  $\beta$  is the order parameter critical index). We find that  $\beta \approx 0.79$  for the mixture with 4.5 mol% BC molecules and 0.56 for the mixture with 8 mol% BC molecules. One would have expected that the ordering transition should follow the  $xy$  model, in which case  $\beta$  should be  $\sim 0.35$  (17). We believe that the higher measured values reflect the fact that the phase diagram of  $T_{ub}$  versus concentration (Fig. 2) tends to have an almost vertical slope at lower concentrations of the BC molecules. It is known from studies of systems showing re-entrant phases (18) that the critical index could then double for essentially geometric reasons. As the concentration of the BC compound increases, the index  $\beta$  decreases. However, the concentration range over which the  $\text{SmA}_{2b}$  phase occurs is relatively small, and the slope of the transition line is not small enough to get the expected  $xy$  value.

It would be interesting to look for this transition in other systems with the hope of widening the range of occurrence of the biaxial smectic phase. It would then be possible to study many physical properties of the system, which has an almost ideal  $xy$  character. A similar transition could occur in bilayer membranes, in which the strong fluctuations of the two-dimensional system can be expected to have a bearing on the problem.

#### References and Notes

1. P. G. de Gennes and J. Prost, *The Physics of Liquid Crystals* (Clarendon, Oxford, 1993).
2. S. Chandrasekhar, *Liquid Crystals* (Cambridge Univ. Press, Cambridge, 1992).
3. C. Robinson, *Disc. Faraday Soc.* **25**, 29 (1958).
4. R. Pratibha and N. V. Madhusudana, *Mol. Cryst. Liq. Cryst. Lett.* **1**, 111 (1985).
5. P. Pallffy-Muhoray, J. R. de Bruyn, D. A. Dunmur, *Mol. Cryst. Liq. Cryst.* **127**, 301 (1985).
6. H. R. Brand, P. E. Cladis, H. Pleiner, *Macromolecules*

- 25**, 7223 (1992). The biaxial  $\text{SmA}$  phase is called the  $C_m$  phase by Brand *et al.* Theoretical discussions can also be found on the influence of molecular biaxiality on the uniaxial  $\text{SmA-N}$  transition [E. M. Averyanov and A. N. Primak, *Liq. Cryst.* **13**, 139 (1993)] and on the roto-translational diffusion in  $\text{SmA}$  [A. Brognara, P. Pasini, C. Zannoni, *J. Chem. Phys.* **112**, 4836 (2000)].
7. H. F. Leube and H. Finkelmann, *Makromol. Chem.* **192**, 1317 (1991).
8. T. Niori, T. Sekine, J. Watanabe, T. Furukawa, H. Takezoe, *J. Mater. Chem.* **6**, 1231 (1996).
9. D. R. Link *et al.*, *Science* **278**, 1924 (1997).
10. G. Heppke and D. Moro, *Science* **279**, 1872 (1998).
11. H. R. Brand, P. E. Cladis, H. Pleiner, *Europhys. J. B*, **6**, 347 (1998); A. Roy, N. V. Madhusudana, P. Toledano, A. M. Figueiredo Neto, *Phys. Rev. Lett.* **82**, 1466 (1999).
12. G. Pelzl, S. Diele, W. Weissflog, *Adv. Mater.* **11**, 707 (1999). We follow the nomenclature  $B_1 \dots B_7$  as given by Pelzl *et al.* for phases exhibited by BC molecules.
13. B. K. Sadashiva, *Mol. Cryst. Liq. Cryst.* **55**, 135 (1979); ———, V. A. Raghunathan, R. Pratibha, *Ferroelectrics*, in press.
14. Supplementary material is available at *Science Online* ([www.sciencemag.org/feature/data/1049282.shl](http://www.sciencemag.org/feature/data/1049282.shl)).
15. Note that all the transition lines between different

- B phases are essentially vertical in Fig. 2. Observations on contact preparations between compositions on either side of the appropriate transition line show two phase regions. The islands of one phase in the background of the other neither grow nor shrink with temperature. The potential energy minima corresponding to the  $\text{SmA}_b$ ,  $B_6$ ,  $B_1$ , and  $B_2$  phases are separated by large barriers.
16. Defects (called dispirations) of strength  $1/2$  can also occur if successive bilayers as in Fig. 4A have an antiferroelectric ordering of the BC molecules, and the disclination is associated with a screw dislocation with a Burgers vector of magnitude  $2l$  [Y. Takanishi, H. Takezoe, A. Fukuda, J. Watanabe, *Phys. Rev. B* **45**, 7684 (1992)]. In our sample of  $\text{SmA}_{2b}$ , defects of strength 1 often split to form two defects of strength  $1/2$ , which is not seen in dispirations. Further, we did not find any switching due to polarization when a dc electric field up to 5 V/ $\mu\text{m}$  applied in the layer plane was reversed. Also, we did not see six- and eight-brush defects often seen in antiferroelectrics.
17. C. Domb, *The Critical Point* (Taylor and Francis, London, 1996), p. 349.
18. T. Narayanan and A. Kumar, *Phys. Rep.* **249**, 135 (1994).

8 February 2000; accepted 3 May 2000

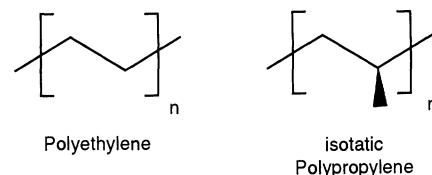
## High-Strength Welds in Metallocene Polypropylene/Polyethylene Laminates

Kimberly A. Chaffin,<sup>1\*</sup> Jeffrey S. Knutsen,<sup>1</sup> Patrick Brant,<sup>2</sup> Frank S. Bates<sup>1†</sup>

Spectacular advances in organometallic chemistry over the past two decades have resulted in single-site catalysts that are revolutionizing production of polyethylene (PE) and isotactic polypropylene (iPP). This report describes an unanticipated benefit of metallocene-catalyzed semicrystalline polyolefins, namely welded joint strengths in PE/iPP laminates that can exceed the cohesive strength of the constituents. We propose that interfacial polymer entanglements, established in the molten state and subsequently anchored in chain-folded lamellae upon crystallization, are responsible for this intrinsic property. The poor adhesion exhibited by traditional Ziegler-Natta-catalyzed polyolefins is shown to derive from the accumulation of amorphous polymer, a by-product of the polymerization reactions, at the interface. These results should facilitate fabrication and improve the properties of composites based on materials that dominate the plastics industry.

Polypropylene (PP) is the thermoplastic polymer with the fastest expansion in production in the world, with an average annual growth rate of 9% since 1991 (1). Currently, worldwide PP resin production is estimated at over 20 million metric tons (1). The vast majority of products are fabricated with iPP, a stereo-

regular macromolecule (Scheme 1) that crystallizes into chain-folded lamellae that melt at about 165°C. This material is used in a plethora of durable and nondurable goods (2) such as food packaging, automobile battery cases, and child car seats. PE is the most widely used plastic (2), with applications ranging



Scheme 1.

<sup>1</sup>Department of Chemical Engineering and Materials Science, University of Minnesota, Minneapolis, MN 55455, USA. <sup>2</sup>Exxon Chemical Company, Baytown Polymers Center, Baytown, TX 77522, USA.

\*Present address: Medtronic, Materials and Biosciences Center, Brooklyn Center, MN 55430, USA. †To whom correspondence should be addressed. E-mail: bates@cems.umn.edu

from exquisitely engineered artificial knees and hips to cheap grocery bags. In 1998, over 43 million metric tons were produced, which translates to a global consumption rate of 8 kg per person per year (3). Numerous grades of PE are marketed, including high and low density (HDPE and LDPE) and many varieties of linear low density (LLDPE). Density reflects the percentage of crystallinity, a key factor in establishing overall mechanical properties.

This phenomenal growth in production and product diversification of polyolefins has been fueled in part by the implementation of new single-site catalysts such as metallocenes (4). These organometallic compounds afford exceptional control over chain architecture, including manipulation of stereo defects in *i*PP and efficient uniform placement of short and long branches at specific sites in PE, both critical factors in controlling the degree of crystallinity. Moreover, metallocene polymerization chemistry results in substantially narrower molecular weight distributions and virtually eliminates certain spurious side reactions that plague conventional heterogeneous Ziegler-Natta reactions (5, 6).

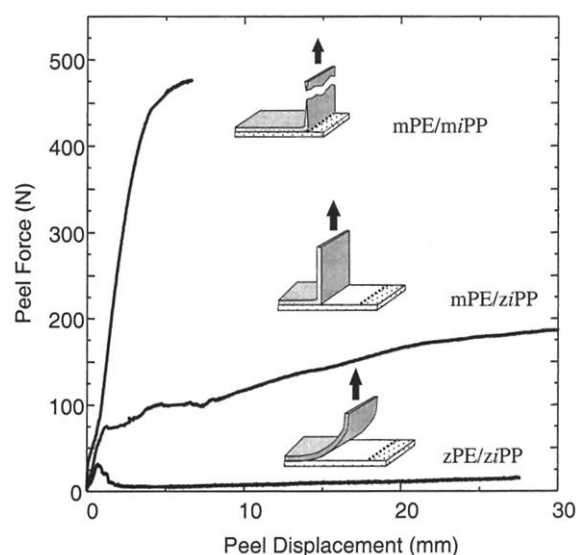
Much emphasis in polyolefin development has been placed on designing new catalysts for higher yields and enhanced stereospecificity (7–9). A sophisticated yet practical understanding of the complex relations between metal center and ligand size, shape, and coordination that control insertion of olefins into the growing polymer molecule has emerged (10–12). The consequences on product mechanical properties have received less attention (13). This report describes a previously unrecognized beneficial consequence of metallocene chemistry on an important physical property of polyolefins: interfacial strength in solid laminates.

Despite the fact that *i*PP and PE are simple chemical isomers, these two polymers are thermodynamically incompatible, even in the molten state. Mechanically mixed or solvent cast blends phase separate and coarsen into discrete phases when the component molecular masses are greater than just a few thousand daltons. When cooled, each phase solidifies by chain-folding into extended crystalline lamellae sandwiched between amorphous regions composed of disorganized looping sections of polymer. PE and *i*PP have different crystal structures, and there is no tendency for cocrystallization (14). Macroscopic pieces of Ziegler-Natta *i*PP and PE generally form weak joints, which can be rationalized on the basis of immiscibility and a low work of adhesion, typical of saturated hydrocarbons.

While investigating the interfacial properties of molded sheets of *i*PP and PE (Table 1), we discovered a remarkable variability in adhesive strength that can be traced back to

the polymerization catalysts. Welds formed between Ziegler-Natta-based *i*PP and PE (denoted *zi*PP and *z*PE) were extremely weak, whereas the joint strength for metallocene *i*PP and PE (referred to as *mi*PP and *m*PE) exceeded the bulk tear strength of the PE film. Force versus displacement curves quantify this effect (Fig. 1). Each curve represents point-by-point averages of at least four different peel test experiments. The *m*PE/*mi*PP laminates display qualitatively different failure behavior than the *z*PE/*zi*PP ones. Application of force resulted in the propagation of a crack along the *z*PE/*zi*PP interface that ultimately led to complete film separation. In fact, there was insufficient adhesion to create a sharp 90° angle at the crack tip (Fig. 1). Conversely, the joint between the *m*PE and *mi*PP was so strong that every attempt to peel these polymers apart resulted in cohesive PE failure (tearing) before development of a crack at the weld line. A series of mixed laminates, formed from *m*PE and *zi*PP, generated an intermediate result (Fig. 1). In this case, a 90° angle of peel was sustained as the crack progressed along the weld.

Clearly, semicrystalline metallocene poly-



olefins produce much stronger welds than the analogous Ziegler-Natta materials. We searched for the cause of these differences using transmission electron microscopy (TEM). Laminate specimens were microtomed to a flat face at -70°C and then stained with ruthenium tetroxide vapor for 6 hours and sectioned into 80-nm-thick slices (15). TEM images were obtained with a JEOL1210 microscope operated at 120 keV. Two representative images, obtained from the interfacial regions of *z*PE/*zi*PP and *m*PE/*mi*PP specimens, are shown in Fig. 2. Contrast is created by differing degrees of absorption of the heavy metal stain in the material: Crystalline regions almost completely exclude the RuO<sub>4</sub> and appear light in these images. White streaks (about 10 nm wide) in both the PE and *i*PP regions correspond to chain-folded crystalline lamellae. Because the PE phases have a lower overall degree of crystallinity (Table 1), they appear darker than the *i*PP domains. At first glance, the morphology of the two specimens appears to be indistinguishable. However, careful inspection reveals a critical difference in the interfacial structure. The *m*PE/*mi*PP interface

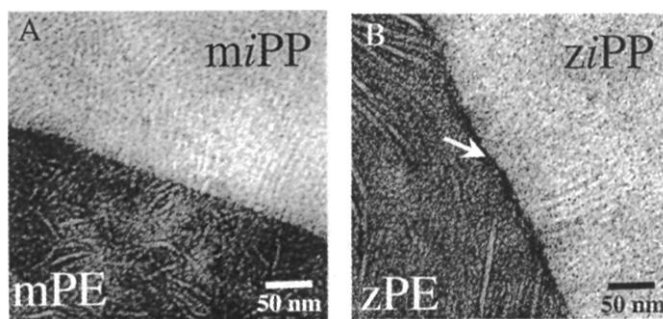
olefins produce much stronger welds than the analogous Ziegler-Natta materials. We searched for the cause of these differences using transmission electron microscopy (TEM). Laminate specimens were microtomed to a flat face at -70°C and then stained with ruthenium tetroxide vapor for 6 hours and sectioned into 80-nm-thick slices (15). TEM images were obtained with a JEOL1210 microscope operated at 120 keV. Two representative images, obtained from the interfacial regions of *z*PE/*zi*PP and *m*PE/*mi*PP specimens, are shown in Fig. 2. Contrast is created by differing degrees of absorption of the heavy metal stain in the material: Crystalline regions almost completely exclude the RuO<sub>4</sub> and appear light in these images. White streaks (about 10 nm wide) in both the PE and *i*PP regions correspond to chain-folded crystalline lamellae. Because the PE phases have a lower overall degree of crystallinity (Table 1), they appear darker than the *i*PP domains. At first glance, the morphology of the two specimens appears to be indistinguishable. However, careful inspection reveals a critical difference in the interfacial structure. The *m*PE/*mi*PP interface

Table 1. Polyolefin molecular characteristics.

Polymer*	Trade name†	$M_n$ ‡ (kg/mol)	$M_w/M_n$ ‡,§	Crystallinity   (weight percent)	Noncrystallizable polymer (weight percent)¶
<i>z</i> PP	PP4062	57	2.4	52 ± 2	0.5
<i>mi</i> PP	Achieve 3825	39	2.0	51 ± 1	<0.2
<i>z</i> PE	LL3003	50	5.5	38 ± 2	5.5
<i>m</i> PE	Exceed 350D60	50	2.3	41 ± 2	<0.5

\*Ziegler-Natta (*z*) and metallocene (*m*) isotactic polypropylene (*i*PP) and polyethylene (PE). †Exxon Chemical Company. ‡Number ( $M_n$ )- and weight ( $M_w$ )-averaged molecular masses. §Manufacturer's estimate from Melt Flow Index (PE) or Melt Flow Rate (*i*PP). ||Determined by wide angle x-ray scattering. ¶Determined by TREF (18).

**Fig. 2.** TEM images of the interfacial region in welded PE/*i*PP laminates. The metallocene-based polymers (A) exhibit a relatively sharp phase boundary virtually free of non-crystallizable material. In contrast, the interface between the welded Ziegler-Natta-based plastics (B) contains a heavily stained band, about 10 nm wide (arrow), indicating that amorphous material has collected at the phase boundary.



(Fig. 2A) shows a clean transition from one phase to the other, with lamellae evident right up to the juncture, even protruding across the boundary in places. In contrast, there is a distinct band of black stained material, about 10 nm wide, separating the zPE and ziPP phases (Fig. 2B). On the basis of the staining characteristics, this must be amorphous polymer.

Reference to Table 1 reveals the source of this disparity. Both Ziegler-Natta polymers contain substantially higher amounts of non-crystallizable material than the corresponding metallocene compounds (16). This difference is marked for the PEs, where 5.5% of the zPE is noncrystallizable, whereas less than 0.5% of the mPE falls in this category. This amorphous material tends to accumulate at the phase boundary for at least two reasons. In the molten state, it may lower the interfacial tension (17, 18), whereas during crystallization, these impurities can be swept to the weld through a process analogous to zone refining (19). We have not established which of these mechanisms contributes most of the deposition of the amorphous polymer at the interface.

These experimental results allow us to propose a model for interfacial strengthening in semicrystalline polymer welds. Development of interfacial structure begins at elevated temperatures where both polymers are melted. Well-established thermodynamic concepts permit us to estimate an interfacial thickness of  $a_1 \approx 4$  nm between PE and *i*PP melts (20, 21) (this short-range dimension is not very sensitive to variations in chain architecture that result from the use of different catalysts). This thickness is sufficient to permit molten PE and *i*PP chains to entangle at the interface (22).

Entanglements are the most important molecular factor in determining polymer properties in the melt and solid states. For example, entangled glassy polystyrene is a relatively tough plastic, whereas the unentangled version is brittle and useless. Entangled PE finds myriad uses as a tough plastic, whereas unentangled PE has the properties of candle wax. In the molten state, entangled polymers are viscoelastic, whereas unen-

tangled ones are simple liquids. Addition of block copolymers to phase-separated glassy polymers (such as polystyrene and polymethylmethacrylate) as blends (23) or laminates (24, 25) enhances interfacial strength provided that each block entangles with the respective homopolymers.

The onset of entanglement behavior in polymers occurs at a well-defined molecular mass,  $M_e$ . Polyethylene has the lowest value of all known polymers,  $M_{e,PE} = 1,000$  g/mol, whereas for *i*PP,  $M_{e,PP} = 5,000$  g/mol (26). On the basis of documented values for the random walk statistical dimensions of molten PE and *i*PP chains (26), an entanglement length will span an average distance of 1.5 and 2.2 nm, respectively. Thus, PE and *i*PP molecules will form numerous topological entanglements as they weave back and forth across the molten phase boundary (Fig. 3A). This model of interfacial entanglement mimics theories developed in the 1980s to explain crack healing in amorphous polymers (27–29).

Cooling and subsequent crystallization lead to the incorporation of most of the metallocene polymer chains emanating from the interfacial region into chain-folded lamellae (Fig. 3B). This stitches together the mPE and *m*iPP films with anchored entanglements. We believe this mechanism to be responsible for the remarkable weld strength displayed by the metallocene polyolefin laminates [this explanation relies on the same principles that account for weld strength in glassy polymers (27–29), where entanglements are immobilized by vitrification rather than crystallization (30)]. These experiments confirm our previous speculation regarding the origin of low-temperature fracture strength improvement documented in metallocene PE-modified PPs (21).

Why is this entanglement mechanism operative with conventional Ziegler-Natta polyolefins? We believe that the amorphous material that accumulates at the zPE/ziPP interface eliminates entanglement coupling by separating and disengaging the PE and *i*PP crystalline domains (Fig. 3C). The resulting weld, composed of rubbery material and lacking anchored entanglements, is incapable

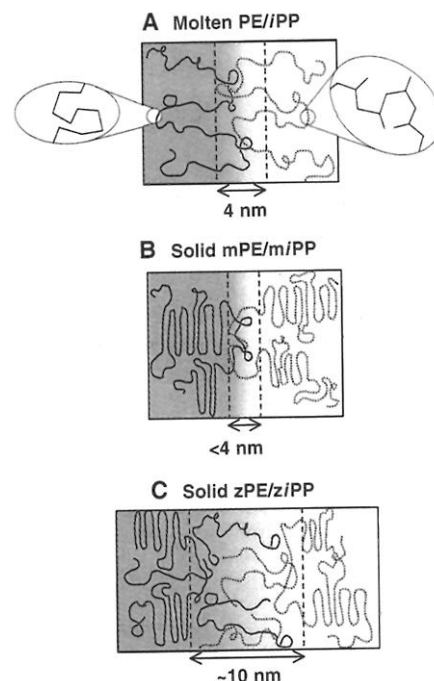


**Fig. 3.** Postulated mechanism for high-strength welding of semicrystalline polyolefins. (A) Equilibrium interfacial structure between molten PE and *i*PP. The estimated interfacial thickness (4 nm) will support molecular entanglements between the phase-separated components. Crystallization of the metallocene laminate (B) anchors interfacial entanglements in chain-folded lamellae, resulting in a mechanically tough weld. Amorphous polymer, a by-product of the polymerization reaction, accumulates at the interface of the welded Ziegler-Natta films (C), decoupling interfacial entanglements leading to poor peel strength. This amorphous material is preferentially stained and appears as a black band at the zPE/ziPP interface in Fig. 2B.

of supporting a load. Peel strengths similar to those for mPE/ziPP and zPE/ziPP (Fig. 1) have been reported for other semicrystalline polyolefin laminates (31).

Product development increasingly relies on multicomponent composites that must be fabricated through the formation of sturdy joints. Our discovery of anchored entanglement interfacial strengthening provides a simple and effective way to weld semicrystalline polymers, which will impact numerous technologies, whether the fabrication requires macroscopic welding as shown herein or blending as demonstrated elsewhere (21).

**References and Notes**

1. A. Jebens, "Polypropylene resins," Chemical Economics Handbook (CEH) Report (SRI International, Menlo Park, CA, 1997) (available at <http://ceh.sric.sri.com/Public/Reports>).
2. N. J. Maraschin and R. C. Miller, *Modern Plastics* **74** (no. 13), 33 (1997).
3. A. Jebens, "High density polyethylene resins," Chemical Economics Handbook (CEH) Report (SRI International, Menlo Park, CA, 1999) (available at <http://ceh.sric.sri.com/Public/Reports>).
4. W. Kaminski, *Makromol. Chem.-Rapid* **4**, 417 (1983).
5. J. C. Stevens, *Stud. Surf. Sci. Catalysis* **101**, 11 (1996).

6. R. F. Service, *Science* **278**, 33 (1997).
7. E. J. Beckman, *Science* **283**, 946 (1999).
8. S. B. Roscoe, J. M. J. Fréchet, J. F. Walzer, A. J. Dias, *Science* **280**, 270 (1998).
9. G. W. Coates and R. M. Waymouth, *Science* **267**, 217 (1995).
10. T. R. Younkin et al., *Science* **287**, 460 (2000).
11. F. C. Stehling, U.S. Patent 5,008,204 (1991).
12. J. C. Stevens, U.S. Patent 5,064,802 (1991).
13. H.-H. Shih, C.-M. Wong, Y.-C. Wang, C.-J. Huang, C.-C. Wu, *J. Appl. Polym. Sci.* **73**, 1769 (1999).
14. J. C. Whittmann and B. Lotz, *Prog. Polym. Sci.* **15**, 909 (1990).
15. G. M. Brown and J. H. Butler, *Polymer* **38**, 3937 (1997).
16. The noncrystallizable portion of the zPE polymer was determined to be relatively low molecular mass ( $M_w \approx 30,000$  daltons) and highly branched material (more than 14% branched repeat units) as determined by temperature rising elution fractionation (TREF) [L. Wild, T. R. Ryle, D. C. Knobloch, I. R. Peat, *J. Polym. Sci. Polym. Phys. Ed.* **20**, 441 (1982)] and gel permeation chromatography (GPC).
17. D. Broseta, G. H. Fredrickson, E. Helfand, L. Leibler, *Macromolecules* **23**, 132 (1990).
18. S. H. Anastasiadis, I. Gancar, J. T. Koberstein, *Macromolecules* **21**, 2980 (1988).
19. D. C. Bassett, *Principles of Polymer Morphology* (Cambridge Univ. Press, New York, 1981).
20. E. Helfand and A. Sapse, *J. Chem. Phys.* **62**, 1327 (1975).
21. K. A. Chaffin, F. S. Bates, G. M. Brown, P. Brant, *J. Polym. Sci. Polym. Phys.* **38**, 108 (2000).
22. Linear dynamic mechanical spectroscopy measurements indicate that all PE and iPP polymer chain relaxation times are less than 0.1 s at the laminate molding temperature. Hence, the 10-min molding time far exceeds the time required to achieve an equilibrium interfacial composition profile.
23. C. Creton, E. J. Kramer, G. Hadziioannou, *Macromolecules* **24**, 1846 (1991).
24. H. R. Brown, *Macromolecules* **22**, 2859 (1989).
25. \_\_\_\_\_, V. R. Deline, P. F. Green, *Nature* **341**, 221 (1989).
26. L. J. Fetters, D. J. Lohse, D. Richter, T. A. Witten, A. Zirkel, *Macromolecules* **27**, 4639 (1994).
27. Y. H. Kim and R. P. Wool, *Macromolecules* **16**, 1115 (1983).
28. D. Adolf, M. Tirrell, S. Prager, *J. Polym. Sci. Polym. Phys.* **23**, 413 (1985).
29. H. H. Krausch and M. Tirrell, *Annu. Rev. Mater. Sci.* **26**, 651 (1989).
30. Because molecular conformations are perturbed by crystallization, PE/iPP weld strength may be affected by laminate cooling rate, as shown by Lin et al. (32). Experiments with mPE/mPP laminates confirm that peel strength decreases with decreasing cooling rate. This is not a consequential factor with glassy polymers because vitrification is essentially uncorrelated with chain conformation.
31. Peel tests on laminated films of Ziegler-Natta iPP and ethylene-propylene (block) copolymer (32) resulted in adhesive strengths comparable to those reported here for the Ziegler-Natta polymers, that is, more than an order of magnitude lower than the failure strength of the all-metalocene materials.
32. G. Lin, W. Wenig, J. Petermann, *Angew. Makromol. Chem.* **255**, 33 (1998).
33. Financial support was provided to the University of Minnesota by the Exxon Chemical Company. TEM and x-ray scattering measurements were conducted at the University of Minnesota Materials Research Science and Engineering Center-supported Institute of Technology Characterization Facility.

20 March 2000; accepted 4 May 2000

## Understanding the Distribution of Near-Earth Asteroids

William F. Bottke Jr.,<sup>1</sup> Robert Jedicke,<sup>2</sup> Alessandro Morbidelli,<sup>3</sup> Jean-Marc Petit,<sup>3</sup> Brett Gladman<sup>3</sup>

We have deduced the orbital and size distributions of the near-Earth asteroids (NEAs) by (i) numerically integrating NEAs from their source regions to their observed orbits, (ii) estimating the observational biases and size distribution associated with asteroids on those orbits, and (iii) creating a model population that can be fit to the known NEAs. We predict that there are ~900 NEAs with absolute magnitude less than 18 (that is, kilometer-sized), of which 29, 65, and 6% reside on Amor, Apollo, and Aten orbits, respectively. These results suggest that roughly 40% of the kilometer-sized NEAs have been found. The remainder, on highly eccentric and inclined orbits, are more difficult to detect.

Most NEAs [definition in (1)] are believed to be fragments of main belt asteroids that, after ejection in a collision event involving a larger asteroid millions of years ago, wandered through space until reaching an Earth-approaching orbit (2). Evidence from the lunar and terrestrial crater record indicates that this population has bombarded Earth over the age of the solar system, and related geologic evidence indicates that the collision of a multi-kilometer asteroid with Earth can wreak regional-to-global devastation on our biosphere (3).

Despite widespread recognition of the NEA impact hazard (4), the distributions of NEA orbits and sizes remain uncertain. As of April 2000, ~950 NEAs have been detected that have absolute magnitude  $H$  between 10

and 29 (5), roughly corresponding to asteroid diameters  $D$  between 40 and 0.01 km (6). It is likely that only NEAs brighter than  $H \sim 14$  ( $D > 7$  km) have been completely discovered (7, 8); these 16 objects are too few to help determine the orbital distribution of the smaller NEAs. An added complication is that the observed distribution of  $H > 14$  NEAs is heavily skewed because (i) they were discovered piecemeal by different asteroid survey programs following a variety of detection strategies; and (ii) each survey is flux-limited, so that the volume of space it investigates varies strongly with  $H$  (9, 10). Even worse, our understanding of the orbital paths taken by bodies to replenish the NEA population is incomplete, making it difficult to use specific NEAs as tracers of large-scale dynamical processes. Interpreting the orbital distribution of the NEA population, therefore, requires a knowledge of the detection biases involved and a characterization of the statistical evolution of NEAs from their sources.

To attack these problems, we constructed a steady-state model of the orbital and size dis-

tributions of the NEAs (11). NEA orbits were generated by tracking the dynamical evolution of test bodies coming out of three so-called intermediate sources (ISs): regions that are constantly fed material escaping the main belt. The relative contributions of the ISs are expressed through weighting coefficients. The NEA size distribution, assumed to be orbit-independent, was constructed so that its shape could be manipulated using a single parameter. Combining these components with the observational biases associated with the Spacewatch NEA survey, we obtained a model distribution (with three adjustable parameters) that could be fit to the orbits and sizes of the NEAs discovered or accidentally rediscovered by Spacewatch. The best-fit parameters extracted from this technique were then used to calculate the debiased NEA population.

The physical and orbital properties of NEAs suggest that many originated in the main belt (2). Asteroid fragments, liberated during collisions in the main belt, are directly injected (12) or slowly moved via Yarkovsky thermal drag (13) into both mean-motion resonances with the planets and so-called secular resonances, where orbital frequencies are commensurate with the solar system's natural frequencies (14). These mechanisms create three important ISs for the NEAs: (i) asteroids in the 3:1 mean-motion resonance with Jupiter; (ii) asteroids in the  $\nu_6$  secular resonance; and (iii) asteroids on Mars-crossing orbits adjacent to the main belt, which have not yet entered the NEA region. The eccentricities (and inclinations) of the IS asteroids are modified by resonant perturbations and/or planetary encounters until they reach the NEA region (15–17). Other potential IS regions (for example, asteroids in the 5:2 resonance with Jupiter) provide relatively few NEAs (18).

To understand the orbital paths followed

<sup>1</sup>Center for Radiophysics and Space Research, Cornell University, Ithaca, NY 14853–6801, USA. <sup>2</sup>Lunar and Planetary Laboratory, University of Arizona, Tucson, AZ 85721, USA. <sup>3</sup>Observatoire de la Côte d'Azur, Boite Postale 4229, 06034 Nice Cedex 4, France.

To whom correspondence should be addressed. E-mail: bottke@astro.sun.tn.cornell.edu